


Unifying fluidization and defluidization of granular columns

L. Chupin¹, O. Roche², and S. van den Wildenberg^{2,3,*}

¹*Université Clermont Auvergne, CNRS UMR 6620, Laboratoire Mathématiques Blaise Pascal, F-63000 Clermont-Ferrand, France*

²*Université Clermont Auvergne, CNRS, IRD, OPGC, Laboratoire Magmas et Volcans, F-63000 Clermont-Ferrand, France*

³*Université Clermont Auvergne, CNRS, Laboratoire de Physique de Clermont Auvergne, F-63000 Clermont-Ferrand, France*

 (Received 14 October 2024; revised 28 January 2025; accepted 2 April 2025; published 18 April 2025)

We study air pressure during the fluidization and defluidization of granular columns with the aim to unify the description of these processes. To this end, we perform experiments with different air flow velocities and columns of different heights. The experimental measurements evidence a nonlinear relationship between pressure and the depth in the column. This complex pressure profile challenges the conventional framework of Darcy's law, typically used to analyze airflow in granular columns. We introduce a law that effectively captures these nonlinear effects, occurring even at low particle Reynolds numbers. An advantage of our approach is its applicability to defluidization—a key phenomenon in gravity-driven gas-particle flows. Using this law, we present a model to describe the decrease of air pressure in a defluidizing column, with numerical simulations aligning well with experimental results.

DOI: [10.1103/PhysRevE.111.045421](https://doi.org/10.1103/PhysRevE.111.045421)

I. INTRODUCTION

The interstitial gas in granular mixtures plays an important role in many industrial and geophysical processes. If the pore gas pressure is high, the effective friction is reduced and the flow of such mixtures is fluidlike. Instead, if the pore pressure is negligible the mixture will flow like a dry granular material [1]. To accurately predict the behavior of gas-particle mixtures, it is thus important to understand the gas solid interactions. The basic law governing the laminar flow of a fluid through a porous media, such as an ensemble of grains, is Darcy's law. If the flow is directed in the direction denoted z then this law predicts a proportionality between the pressure gradient $\partial_z P$ and the velocity U of the flow in this direction:

$$\frac{\partial P}{\partial z} = -\frac{\mu}{k}U. \quad (1)$$

The coefficient depends on the dynamic viscosity of the fluid μ and the permeability of the granular medium k . Note that U is the superficial fluid velocity, or, in other words, a macroscopic averaged velocity. For flows through porous media with higher particle Reynolds numbers, inertial effects may become significant. In this flow regime, the Darcy-Forchheimer equation captures the nonlinear behavior of the pressure gradient as a function of flow velocity [2,3]:

$$\frac{\partial P}{\partial z} = -\frac{\mu}{k}U + \frac{\rho}{k_1}U^2 \quad (2)$$

with the fluid density ρ and the inertial permeability k_1 .

For monosize beads, the permeabilities in the viscous and inertial regime can be obtained from the solid volume fraction ϕ , and the diameter d and sphericity θ of the particles, see [4]:

$$k = \frac{\theta^2 d^2 (1 - \phi)^3}{150 \phi^2} \text{ and } k_1 = \frac{\theta d (1 - \phi)^3}{1.75 \rho \phi}.$$

The fluidization of granular media is principally characterized via the minimum fluidization velocity U_{mf} , which is defined as the superficial fluid velocity at which there is a transition from a fixed bed to a fully fluidized state. Multiple studies have developed empirical and semiempirical correlations of U_{mf} [5–9].

In contrast to fluidization, the defluidization process, in which the fluid escapes from the granular bed, is much less studied. Nevertheless, defluidization is important in many natural systems since the fluid is not continuously supplied. An important question is thus how the fluid pressure in such systems decreases over time. Indeed, it was shown that diffusion laws can quantitatively describe the time evolution of pore fluid pressure, but the inferred diffusion coefficient increases with the height of the granular column [1,10]. It was suggested that this effect is simply due to the extra volume of air below the bed in the so-called windbox [10]. However, as we will show, it occurs even when the extra volume is negligible compared to the volume of interstitial gas in the bed.

We performed careful experiments on the fluidization and defluidization of granular columns of different heights. We show that the fluid pressure profile increases nonlinearly inside the granular bed contrary to predictions by Darcy's law. We capture this effect by extending Darcy's law with a linear pressure term. This simple extension permits us to easily rewrite the law in terms of the fluid flow and test our model in defluidization experiments. We find good agreement between experimentally measured pressure decays and the extended Darcy's law.

II. EXPERIMENTAL METHODS

Experiments were performed in a plexiglass cylindrical pipe with inner diameter $D = 0.14$ m and a height of 2 m [Fig. 1(a)]. At the bottom of the pipe was a porous plate (W) and the ensemble was placed on top of a chamber called the

*Contact autor: siet.van_den_wildenberg@uca.fr

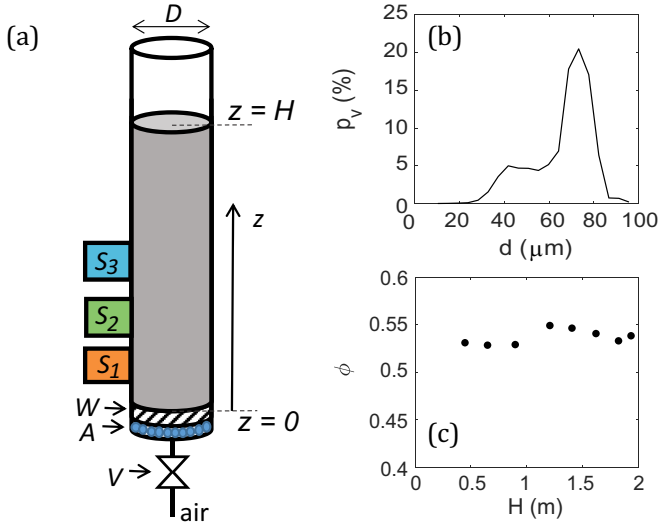


FIG. 1. (a) Schematic diagram of the experimental setup, a cylinder placed on a porous plate W and a windbox A . Pressure sensors S_i are located at positions $z_1 = 0.04$ m, $z_2 = 0.13$ m, and $z_3 = 0.3$ m. Air flow is controlled by a solenoid valve V . (b) Particle size distribution with d the equivalent circle diameter (diameter of a circle with the same area as the projected area of the particle image) and p_v the volume fraction in each bin. (c) Solid volume fraction ϕ versus the height of the column H .

windbox (A) with the same inner diameter as the pipe. The porous plate had a thickness of 5 mm and a pore size of 20 μm . The windbox and the porous plate are essential to ensure uniform airflow within the granular column. The “extra volume” of air refers to the air trapped in the windbox (between the valve and the granular column). When the valve is closed, this trapped air must escape through the column, which can delay and alter the pressure evolution if its volume is significant compared to the air volume in the column. Therefore, it is important to minimize the wind-box volume, which we achieved by filling it with glass beads ($d = 1.5$ mm). The volume of air in the windbox and the porous plate was estimated to be approximately $4.8 \times 10^{-5} \text{ m}^3$, which corresponded to about 0.1% of the volume of air in the smallest granular column tested here. Taking a permeability of the porous plate of $k_{\text{plate}} \approx 10^{-11} \text{ m}^2$ and $\phi_{\text{plate}} \approx 0.5$, the pressure drop over the plate was estimated to be of order of 52 Pa for the highest air flow tested.

A laboratory air supply system delivered mean air flow velocities (U) through the windbox and the porous plate into the pipe. The pressure of the interstitial air in the cylinder was measured by three piezoresistive sensors S_1 , S_2 , and S_3 installed at a distance from the porous plate of 0.04 m, 0.13 m, and 0.3 m, respectively. The sensors were placed in adapters so that the front of the sensors was in direct contact with interstitial air via a small hole covered by a grid (36 μm mesh size) to prevent particles from entering the adapter and colliding with the sensors. The back of the sensors were in contact with the atmospheric pressure only. Therefore, the sensors measured the differential pressure between their front and back sides, which corresponded to the pore fluid pressure in the pipe.

We used nearly spherical glass beads of density $\rho = 2500 \text{ kg m}^{-3}$, which were characterized using MORPHOLOGY G3SETM equipment from Malvern InstrumentTM following the protocol of Leibrandt and Le Pennec [11]. The particle size distribution has a tail at smaller particle sizes and, therefore, we consider the Sauter diameter. The Sauter diameter accounts for the importance of drag forces on the particle [12]. For the glass particles, we find a Sauter diameter $d = 62 \mu\text{m}$ and a sphericity $\theta = 0.97$.

To generate reproducible granular packings, we developed a sample preparation protocol as follows. First, a known mass of glass beads was poured into the pipe. Second, to avoid excessive cohesion due to ambient moisture, the glass beads were aerated for about 20 min using a dry air flux at a velocity greater than U_{mf} . Third, the granular bed was expanded using the air flux, after which the air flux was stopped and the bed was compacted by tapping the wall of the container 20 times and the height of the column was measured. In this way, we obtained granular beds with reproducible bulk solid volume fractions $\phi \approx 0.54$ [Fig. 1(b)]. After a granular packing was prepared, a fluidization or defluidization experiment was started.

In the fluidization experiments, the air flow was gradually increased and the fluid pressure was monitored. To ensure that a steady-state fluid pressure was established we waited several minutes before each pressure measurement. For each U , the generated fluid pressure was measured over time by the pressure sensors that each took 500 samples with a sampling rate of ≈ 41 Hz. Next, for each sensor, a time averaged fluid pressure P was calculated by averaging over the 500 samples (≈ 12 s).

In defluidization experiments, to obtain a well defined initial pressure, the pressure measurements started several seconds before the airflow was stopped. A solenoid valve (V) placed at the entrance of the windbox was then used to almost instantaneously (≈ 0.01 s) stop the air flow. To accurately determine the moment the air flow was stopped, corresponding to $t = 0$ in the experiments, an electric signal generated upon closing the valve was used to trigger the acquisition of fluid pressure. The fluid pressure in time was acquired by taking more than 2000 samples at a sampling rate of about 42 Hz. During these experiments the height of the column was monitored using a ruler, and we estimated change of the height to be less than 0.1 %.

III. FLUIDIZATION AND MODEL

We start by investigating the fluidization of granular columns. For this, reproducible granular beds of height H are prepared by loading a known mass of particles ($d = 80 \mu\text{m}$) into the container from the top (for details, see the methods section). Next, an upward vertical air flow is slowly increased until the desired velocity U is reached and then the generated fluid pressure P in the column is measured at three different positions by the differential pressure sensors S_1 , S_2 , and S_3 (Fig. 1). We test eight different column heights ranging from $\approx 0.4 - 2$ m, and for each height we repeat the experiment three times. The pore fluid pressure is then averaged over the three experiments and evaluated as a function of U [Fig. 2(a)]. In general, we observe the well known features of granular

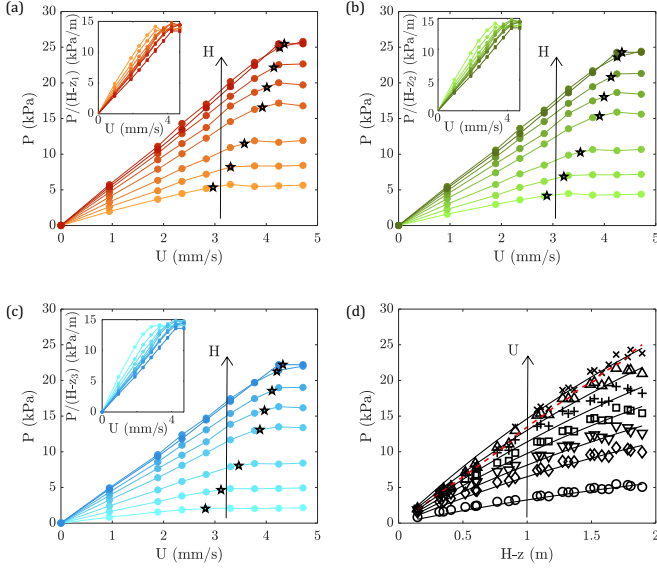


FIG. 2. Pore fluid pressure P versus the air velocity U for different H . (a) P measured by sensor S_1 at position $z_1 = 0.04$ m. (b) P measured by sensor S_2 at position $z_2 = 0.13$ m. (c) P measured by sensor S_3 at position $z_3 = 0.3$ m. Insets are the ratio $P/(H - z_i)$ versus U , showing a clear decrease of the slope for increasing H . Error bars representing the standard error of the mean, obtained over three experiments, are nearly equal or smaller than the symbols. Black stars indicate U_{mf} estimated from the intersect of two linear fits (see Appendix A). (d) Fluid pressure data presented in (a)–(c) as a function of depth in the granular bed. For $U \in \{0.9, 1.9, 2.4, 2.8, 3.3, 3.8, 4.2\} \text{ mm s}^{-1}$, corresponding to circle, diamond, downward triangle, square, plus, triangle, and x-mark symbols, respectively. Solid lines are fits by Eq. (4). The red dashed line is P_ℓ calculated from the bulk ϕ .

column fluidization [1,2], namely, (i) a first regime where the pore pressure increases linearly with U , and (ii) a second regime where the pore pressure reaches a plateau value P_m independent of U . The linear increase of P_m with H is well predicted by the lithostatic pressure $P_\ell(z) = \phi \rho_s g(H - z)$ (see Appendix A). The transition between the two regimes occurs at U_{mf} .

In a simple configuration such as that shown in Fig. 1, Darcy's equation (1) can be used to explicitly deduce the pressure P by noting that the pressure at the top corresponding to $z = H$ is given by $P(H) = 0$ (assuming that the pressure at the top of the column equals the atmospheric pressure). We deduce

$$P(z) = \frac{\mu}{k} U(H - z). \quad (3)$$

This yields that the fluid pressure drop $P(z_i)/(H - z_i)$ obtained at different heights z_i , $i \in \{1, 2, 3\}$ is proportional to U and is independent of H . However, experimentally, it is clear that the pressure drop decreases with the height of the granular column (inset of Fig. 2). In the following analysis we excluded only the data for $U = 4.7 \text{ mm s}^{-1}$ for which nonlinear effects in the granular column—such as air bubbles and material dilation—were observed.

Presenting the fluid pressure data as a function of depth in the granular column for different air velocities [Fig. 2(d)],

highlights a nonlinear fluid pressure profile within the granular bed, which indicates nonhomogeneous fluidization. This suggests that there exists no unique value of U_{mf} to define the global state of fluidization of the bed (see Appendix A). Similarly, Delebarre [3] argued that, for long columns, U_{mf} cannot be considered as a criterion to characterize powders. To capture the entire pressure profiles observed in our experiments, we propose the following empirical relation [Fig. 2(d)]:

$$P(z) = aU \frac{1 - e^{-b(H-z)}}{b}. \quad (4)$$

Here $a = 4 \times 10^6 \text{ Pa s m}^{-2}$ and $b = 0.3 \text{ m}^{-1}$ are global parameters obtained from fitting $P(z)$ across a wide range of U [Fig. 2(d)]. Note that a corresponds to the parameter μ/k of Darcy's law. For our glass particles, $\mu/k \approx 2.2 \times 10^6$, which agrees reasonably well with a obtained from the fits. The parameter $1/b$ can be interpreted as a typical length scale.

The choice of an approximation given by Eq. (4) is no accident and has several advantages:

- (i) It provides the pressure profile over the entire column and shows that the degree of fluidization depends on the position in the column.
- (ii) For small column height, that is, for small values of $H - z$, the linear nature of the Darcy law, given by the profile Eq. (3), is restored.
- (iii) The pressure given by Eq. (4) is the solution of a simple differential equation generalizing the usual Darcy law Eq. (1):

$$\frac{\partial P}{\partial z} = -aU + bP. \quad (5)$$

- (iv) As we shall see later, this model also helps us to understand the defluidization phenomenon.

Although we cannot identify the origin of the nonlinear pressure profile, we note that the inertial term in Eq. (2) should not play a major role. Indeed, experimental conditions indicate that the viscous term in Eq. (2) is ten times greater than the inertial term, consistent with modest particle Reynolds numbers ($\text{Re}_p \leq 0.02$). For comparison, the pre-Darcy regime occurs at significantly lower $\text{Re}_p \approx 10^{-5}$ [13], while the upper limit for the applicability of Darcy's law is typically considered to be $\text{Re}_p \sim 1$ – 10 [14].

Note that Eq. (4) is reminiscent of the Janssen model [15], which could thus be a physical phenomenon involved. However, the characteristic length scale $(1/b) \approx 3 \text{ m}$ is nearly 50 times larger than the Janssen length scale $\lambda = R/(2\mu_w K) \sim 0.14 \text{ m}$, with radius of the container R , the effective wall-particle friction coefficient μ_w , and the earth pressure coefficient K ($\mu_w = 0.5$, $K = 0.5$ are typical values for glass bead assemblies [16]). This suggests that $K\mu_w$ is significantly reduced in our experiments. Since $K = 0$ corresponds to a solid and $K = 1$ to a fluid, we expect K to approach 1 in the fluidized beds, implying a significant decrease in μ_w . Although an important reduction in μ_w has been observed in particle suspensions in water due to lubrication effects [16,17], this effect seems less likely to occur in air because of its different properties, such as lower viscosity and density.

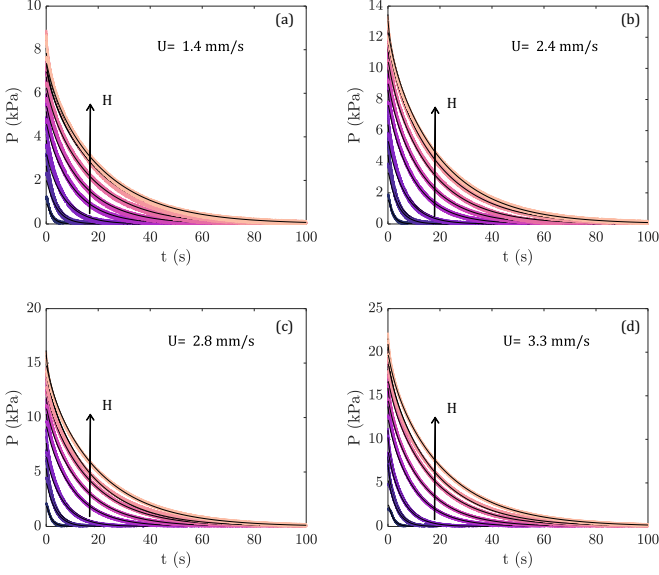


FIG. 3. Representative experiments showing the pore fluid pressure decrease in time, measured using the three pressure sensors for granular columns of increasing height H (from dark purple to light pink and indicated by the arrow). (a) For $U = 1.4 \text{ mm s}^{-1}$, (b) $U = 2.4 \text{ mm s}^{-1}$, (c) $U = 2.8 \text{ mm s}^{-1}$, and (d) $U = 3.3 \text{ mm s}^{-1}$. Solid black lines are fits of Eq. (9).

While we cannot rule out the Janssen effect, we propose that other physical phenomena may also contribute. For example, airflow can alter the particle contact network, potentially through mechanisms such as buckling of force chains [18], leading to hardening of the granular column without changes in packing density. For our glass beads and typical confining pressures (1–10 kPa), Hertz law estimates elastic deformations of the beads to be around 1–5 nm, several orders of magnitude smaller than the grain size. As a result, even tiny deformations can alter the contact network and modify bulk properties, such as force chain lengths and anisotropy, without significantly affecting the macroscopic packing density [19,20]. Consistent with this idea, a previous study has shown that water flow through a confined assembly of photoelastic disks increases the contact force network [21].

IV. DEFLUIDIZATION

To test our model, we now investigate the fluid pressure decay over time. For this, a granular column is first fluidized and subsequently, the air supply is instantly stopped and the decay of fluid pressure is measured in time. Similar to the fluidization experiments discussed before, we vary the height of the column and for each height the experiment is repeated three times. During these experiments, we do not observe any visible rearrangement of the grains nor do we measure any significant change in the height of the granular columns. In general, we find that once the air supply is stopped, the pore fluid pressure in the nonexpanded columns decreases in time, first rapidly and then at a slower rate (Fig. 3). The initial fluid pressure at $t = 0$ as a function of position in the granular bed is well predicted by Eq. (4) [Fig. 4(a)] with a and b deduced from the fluidization experiments.

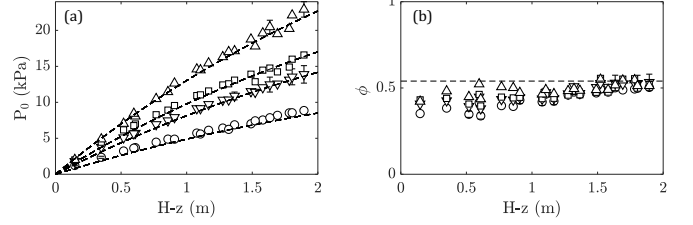


FIG. 4. (a) Initial fluid pressure at $t = 0$'s as a function of position in the granular bed averaged over three defluidization experiments for $U = 1.4, 2.4, 2.8, 3.3 \text{ mm s}^{-1}$ (circle, downward triangle, square, triangle). Error bars representing the standard deviation over three experiments are nearly equal to or smaller than the symbols. Black dashed lines are Eq. (5) with a and b from the fluidization experiments. (b) Solid volume fraction ϕ obtained from fitting the defluidization $P(t)$ by Eq. (9), as a function of position in the column. The dashed line represents $\phi = 0.54$.

The relation for the time-dependent pressure evolution is obtained from the local mass conservation law for the fluid in the column. This relation involves the apparent density $(1 - \phi)\rho$ of the gas, and the microscopic velocity of the gas u . It writes

$$\frac{\partial}{\partial t}((1 - \phi)\rho) + \frac{\partial}{\partial z}((1 - \phi)\rho u) = 0. \quad (6)$$

The link between the microscopic velocity u and the superficial fluid velocity U being given by $U = (1 - \phi)u$, we deduce

$$\frac{\partial}{\partial t}((1 - \phi)\rho) + \frac{\partial}{\partial z}(\rho U) = 0. \quad (7)$$

Assuming an ideal gas, that is the total pressure is proportional to the density: $P_{\text{atm}} + P = \beta\rho$ and the experimental constant $\beta = RT/M(\text{Pa m}^3 \text{ kg}^{-1})$, with the molecular mass of air M , gas constant R , and absolute temperature T . We consider that the solid volume fraction ϕ is constant, and using the extended Darcy's law Eq. (5) derive the law for the evolution of the fluid pressure,

$$\frac{\partial P}{\partial t} + \frac{1}{(1 - \phi)a} \frac{\partial}{\partial z} \left((P_{\text{atm}} + P) \left(bP - \frac{\partial P}{\partial z} \right) \right) = 0. \quad (8)$$

It is therefore relevant to assume that the over-pressure P satisfies $P \ll P_{\text{atm}}$ and neglects some terms (see Appendix B for further details and dimensional analysis). We obtain

$$\frac{\partial P}{\partial t} - \frac{P_{\text{atm}}}{(1 - \phi)a} \frac{\partial^2 P}{\partial z^2} + \frac{P_{\text{atm}}b}{(1 - \phi)a} \frac{\partial P}{\partial z} = 0. \quad (9)$$

Compared with the usual diffusion model based on Darcy's law Eq. (1), which formally corresponds to the case where $b = 0$, we obtain an equation containing an additive first-order term. The experimental pressure evolution is fitted by numerically solving Eq. (9) using MATLAB's `lsqcurvefit` and `ODE45` functions, and ϕ is the only free fitting parameter. The initial condition is given by Eq. (4), corresponding to the steady-state solution for a given velocity U , that is,

$$P(0, z) = aU \frac{1 - e^{-b(H-z)}}{b}. \quad (10)$$

By imposing the following conditions at the top ($z = H$) and bottom ($z = 0$) of the domain,

$$P(t, H) = 0 \quad \text{and} \quad \frac{\partial P}{\partial z}(t, 0) = bP(t, 0), \quad (11)$$

we simulate the stopping of the air injection starting from $t = 0$ [since $U = 0$ corresponds to $\partial_z P = bP$ in the generalized Darcy law Eq. (5)].

We find good agreement between the fits and the experimental defluidization over time for different z , H , and U (Fig. 3). The inferred ϕ , shown in Fig. 4(b), is generally close to the experimentally measured bulk value $\phi \approx 0.54$, and only for the smallest $H - z$ do we observe deviations. This is likely related to a and b , which were obtained from global fits that include fluidization experiments at higher U , where nonlinear phenomena, like particle sliding at the contact scale or the emergence of tiny air bubbles, may come into play.

Importantly, we note that, unlike the diffusion model (see Appendix C), our extended Darcy law-based approach yields a ϕ that appears independent on U and $H - z$.

V. CONCLUSION

Our findings reveal that the fluid pressure profile in fluidized granular columns is nonlinear. This behavior can be captured by an empirical term in Darcy's law. The key advantage of this extended Darcy law is that it can be easily rewritten and used in the derivation of the pressure evolution law, unifying the fluidization and defluidization processes in granular columns.

ACKNOWLEDGMENT

We thank A. Disdier for help with the experiments. This is ClerVolc contribution no. 670.

APPENDIX A: ESTIMATION U_{mf}

For each column height, the minimum fluidization velocity is determined by identifying the intersection point between a linear fit of the data in the regime, where P increases with U , and a fit of the pore pressure in the plateau region [Fig. 5]. The inferred U_{mf} increases with H as observed in [7].

APPENDIX B: DIMENSIONAL STUDY

In this Appendix, we explain the transition from Eq. (8) to its simplified version given by (9). The principle is to justify that certain terms in Eq. (8) are negligible compared to other terms. In order to compare the terms, we must first write a dimensionless version of Eq. (8). To do this, we introduce the following dimensionless variables and unknowns—which will be noted with a \sim symbol:

$$t = T\tilde{t}, \quad z = H\tilde{z}, \quad P = \phi\rho_s g H\tilde{P},$$

where H stands for the characteristic length of the experiment, and T for a characteristic time. Equation (8) can therefore be written as

$$\frac{\partial \tilde{P}}{\partial \tilde{t}} = \tilde{D} \frac{\partial}{\partial \tilde{z}} \left(\frac{\partial \tilde{P}}{\partial \tilde{z}} - \tilde{b}\tilde{P} + \tilde{\varepsilon}\tilde{P} \frac{\partial \tilde{P}}{\partial \tilde{z}} - \tilde{\varepsilon}\tilde{b}\tilde{P}^2 \right), \quad (B1)$$

where \tilde{D} , \tilde{b} , and $\tilde{\varepsilon}$ are three dimensionless numbers given by

$$\tilde{D} = \frac{T p_{atm}}{(1 - \phi)aH^2}, \quad \tilde{b} = bH, \quad \text{and} \quad \tilde{\varepsilon} = \frac{\phi\rho_s g H}{p_{atm}}.$$

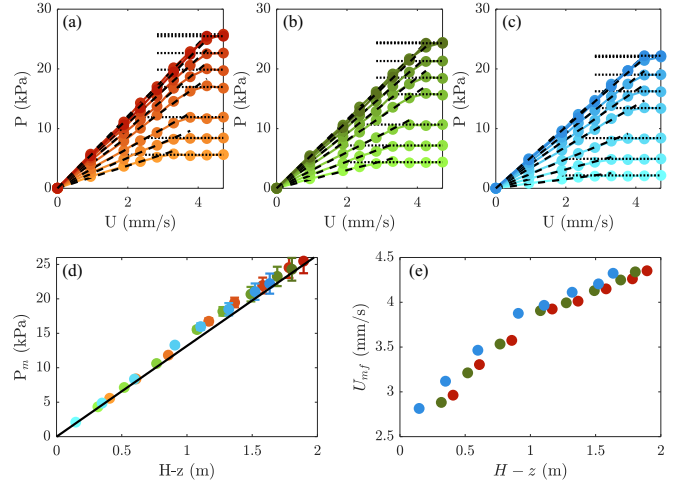


FIG. 5. Pore fluid pressure P versus the air velocity U for different column heights H , same data as Fig. 2 in the main text. (a)–(c) P measured by sensor S_1 , S_2 , and S_3 , respectively, as a function of U . Dashed lines are linear fits to the data in the regime where the pore pressure increases with U . Dotted lines are estimations of the plateau pressure. (d) Maximum fluid pressure P_m obtained from the plateaus in (a)–(c), versus $H - z$. Colors correspond to the colors (a)–(c), and the black line indicates the lithostatic pressure, with the bulk solid volume fraction $\phi = 0.54$. (e) Minimum fluidization velocity U_{mf} estimated from the intersect between the dashed and dotted lines in (a)–(c) as a function of $H - z$.

Thus, depending on the orders of magnitude of the coefficients \tilde{b} and $\tilde{\varepsilon}$, several regimes can be distinguished. Knowing the values $\phi = 0.54$, $\rho_s \approx 2500 \text{ kg m}^{-3}$, $p_{atm} = 10^5 \text{ Pa}$, $b = 0.3 \text{ m}^{-1}$, and $g = 9.8 \text{ m s}^{-2}$, we can separate the cases simply as a function of the height H of the column:

(i) Case $H = 5 \text{ cm}$

$\tilde{b} \approx 1.5 \times 10^{-2} \ll 1$ and $\tilde{\varepsilon} \approx 6.6 \times 10^{-3} \ll 1$ so that (B1) can be reasonably approximated by a simple diffusion equation:

$$\frac{\partial \tilde{P}}{\partial \tilde{t}} = \tilde{D} \frac{\partial^2 \tilde{P}}{\partial \tilde{z}^2}. \quad (B2)$$

In this case, the initial and boundary conditions (10) and (11) can be approximated by

$$\begin{aligned} \tilde{P}(0, \tilde{z}) &= \frac{aU}{\phi\rho_s g} (1 - \tilde{z}) \\ \text{and} \quad \tilde{P}(\tilde{t}, 1) &= \frac{\partial \tilde{P}}{\partial \tilde{z}}(\tilde{t}, 0) = 0 \end{aligned} \quad (B3)$$

so that an explicit solution can be easily obtained by separating the variables and using Fourier series:

$$\begin{aligned} \tilde{P}(\tilde{t}, \tilde{z}) &= \sum_{n=0}^{+\infty} a_n \cos\left(\frac{(2n+1)\pi}{2}\tilde{z}\right) \\ &\times \exp\left(-\left(\frac{(2n+1)\pi}{2}\right)^2 \tilde{D}\tilde{t}\right), \end{aligned} \quad (B4)$$

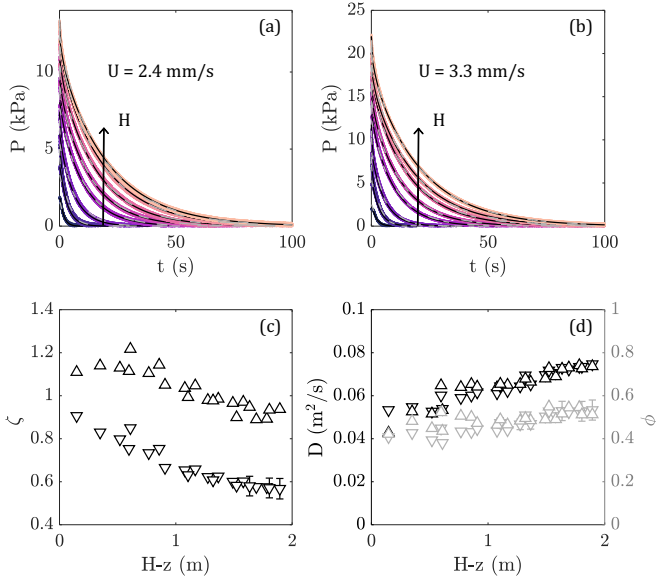


FIG. 6. Fluid pressure versus time for different column heights, same experimental data as in Fig. 3. (a) for $U = 2.4$ mm s⁻¹. (b) $U = 3.3$ mm s⁻¹. Black lines represent fits of (C1). For comparison, the fits using the extended Darcy law model are also shown (gray dashed lines). Both models describe the data for all H and U values equally well. (c) Degree of fluidization ζ obtained from the fits decreases with increasing column height H but increases with U , for $U \in \{2.4, 3.3\}$ mm s⁻¹, corresponding to symbols downward triangle and triangle, respectively. (d) Diffusion constant \mathcal{D} , obtained from the fits, shown as a function of H . For comparison, values of ϕ from Fig. 4(b), are shown in light gray.

where the coefficients a_n , $n \geq 0$, are given using the initial data

$$a_n = \frac{8aU}{\phi \rho_s g(2n+1)^2 \pi^2}. \quad (\text{B5})$$

(ii) Case $H = 40$ cm (order of magnitude of experiments carried out)

$\tilde{b} \approx 1.2 \times 10^{-1}$ and $\tilde{\varepsilon} \approx 5.3 \times 10^{-2} \ll 1$ so that (B1) can be approximated by Eq. (9) (written here in dimensionless

form):

$$\frac{\partial \tilde{P}}{\partial \tilde{t}} = \tilde{\mathcal{D}} \frac{\partial^2 \tilde{P}}{\partial \tilde{z}^2} - \tilde{\mathcal{D}} \tilde{b} \frac{\partial \tilde{P}}{\partial \tilde{z}}. \quad (\text{B6})$$

Note that, although Eq. (B6) remains linear, the boundary conditions (11) do not allow us to obtain a simple analytic expression (using Fourier series, for example) for the solution.

(iii) Case $H = 5$ m

$\tilde{b} \approx 1.5$ and $\tilde{\varepsilon} \approx 6.6 \times 10^{-1}$ and no term in Eq. (8) seems negligible.

APPENDIX C: COMPARISON WITH DARCY'S MODEL

In this section, we compare our model in Eq. (9) for the defluidization of a granular column to a model based on Darcy's law Eq. (1). Following the same procedures as in the main text and Appendix B, we derive the 1D-diffusion equation [1]. In order to complete the model, we need to impose initial conditions corresponding to the situation at the beginning of the experiment, and boundary conditions indicating interactions with the outside. We start with a partially fluidized condition (a proportion $\zeta \in [0, 1]$ of the complete fluidization condition) and assume that at the top of the column the pressure equals the atmospheric pressure, while at the bottom of the column a zero air injection velocity U is imposed:

$$\begin{aligned} \frac{\partial P}{\partial t} &= \mathcal{D} \frac{\partial^2 P}{\partial z^2} \quad \text{for } t > 0 \quad \text{and } z \in (0, H) \\ P(0, z) &= \zeta \phi \rho_s g(H - z) \quad \text{for } z \in (0, H) \\ P(t, H) &= \frac{\partial P}{\partial z}(t, 0) = 0 \quad \text{for } t > 0. \end{aligned} \quad (\text{C1})$$

The pressure evolution is fitted by numerically solving the coupled Eq. (C1) using MATLAB's lsqcurvefit and ODE45 functions, with two free fitting parameters ζ and \mathcal{D} . The fits to the data as well as the inferred parameters are shown in Fig. 6. Generally, we find that both models fit the data similarly well, although the diffusion model uses two parameter optimization in contrast to the single parameter in Eq. (9). The inferred ζ decreases with $H - z$ and increases with U . Importantly, the inferred \mathcal{D} increases about 40% for the $H - z$ tested, consistent with previous observations [1,12].

[1] O. Roche, Depositional processes and gas pore pressure in pyroclastic flows: An experimental perspective, *Bull Volcanol* **74**, 1807 (2012).
[2] D. Geldart, *Gas Fluidization Technology* (Wiley, NY, 1986).
[3] A. Delebarre, Does the minimum fluidization exist? *J. Fluids Eng.* **124**, 595 (2002).
[4] S. Ergun, Fluid flow through packed columns, *Chem. Eng. Prog.* **48**, 89 (1952).
[5] A. Anantharaman, R. A. Cocco, and J. W. Chew, Evaluation of correlations for the minimum fluidization velocity (U_{mf}) in gas-solid fluidization, *Powder Technol.* **323**, 454 (2018).
[6] M. Rasteh, G. Ahmadi, and S. H. Hosseini, Effect of Gaussian size distribution owidth on minimum fluidization velocity in tapered gas-solid fluidized beds, *Particuology* **66**, 71 (2022).

[7] A. Rao, J. S. Curtis, B. C. Hancock, and W. C., The effect of column diameter and bed height on minimum fluidization velocity, *AIChE J.* **56**, 2304 (2010).
[8] H. Quan, N. Fatah, and C. Hu, Diagnosis of hydrodynamic regimes from large to microfluidized beds, *Chem. Eng. J.* **391**, 123615 (2020).
[9] Z. Jiang and N. Fatah, New investigation of microfluidized bed: The effect of wall roughness and particle size on hydrodynamics regimes, *Chem. Eng. J.* **430**, 133075 (2022).
[10] E. Breard, L. Jones, J. and Fullard, G. Lube, C. Davies, and J. Dufek, The permeability of volcanic mixtures-implications for pyroclastic currents, *J. Geophys. Res.: Solid Earth* **124**, 1343 (2019).

- [11] S. Leibbrandt and J. L.-Le Pennec, Towards fast and routine analyses of volcanic ash morphometry for eruption surveillance applications, *J. Volcanol. Geotherm. Res.* **297**, 11 (2015).
- [12] E. C. P. Breard, J. Dufek, and G. Lube, Enhanced mobility in concentrated pyroclastic density currents: An examination of a self-fluidization mechanism, *Geophys. Res. Lett.* **45**, 654 (2018).
- [13] R. M. Fand, B. Y. K. Kim, A. C. C. Lam, and R. T. Phan, Resistance to the flow of fluids through simple and complex porous media whose matrices are composed of randomly packed spheres, *J. Fluids Eng.* **109**, 268 (1987).
- [14] W. Sobieski and A. Trykozko, Darcy's and Forchheimer's laws in practice. Part 1. The experiment, *Tech. Sci.* **17**, 321 (2014).
- [15] H. A. Janssen, Versuche über getreidedruck in silozellen, *Z. Ver. Dtsch. Ing* **39**, 1045 (1895).
- [16] S. M. Brice, M. Georgelin, S. Deville, and A. Pocheau, Wall friction and Janssen effect in the solidification of suspensions, *Soft Matter* **14**, 9498 (2018).
- [17] I. Rosenhek-Goldian, N. Kampf, and J. Klein, Trapped aqueous films lubricate highly hydrophobic surfaces, *ACS Nano* **12**, 10075 (2018).
- [18] J. D. Goddard, Nonlinear elasticity and pressure-dependent wave speeds in granular media, *Proc. R. Soc. London A* **430**, 105 (1990).
- [19] C. F. Schreck, T. Bertrand, C. S. O'Hern, and M. D. Shattuck, Repulsive contact interactions make jammed particulate systems inherently nonharmonic, *Phys. Rev. Lett.* **107**, 078301 (2011).
- [20] E. T. Owens and K. E. Daniels, Sound propagation and force chains in granular materials, *Europhys. Lett.* **94**, 54005 (2011).
- [21] N. Mahabadi and J. Jang, The impact of fluid flow on force chains in granular media, *Appl. Phys. Lett.* **110**, 041907 (2017).